

## **Oscillatory surface deformation of paramagnetic rare earth solutions driven by an inhomogeneous magnetic field**

Fritzsche, B.; Mutschke, G.; Meinel, T.; Yang, X.; Lei, Z.; Eckert, K.;

Originally published:

June 2020

**Physical Review E 101(2020), 062601**

DOI: <https://doi.org/10.1103/PhysRevE.101.062601>

Perma-Link to Publication Repository of HZDR:

<https://www.hzdr.de/publications/Publ-31036>

Release of the secondary publication  
on the basis of the German Copyright Law § 38 Section 4.

## Oscillatory surface deformation of paramagnetic rare earth solutions driven by an inhomogeneous magnetic field

B. Fritzsche,<sup>1, a)</sup> G. Mutschke,<sup>2, b)</sup> T. J. Meinel,<sup>1</sup> X. Yang,<sup>1, 2</sup> Z. Lei,<sup>1, 2</sup> and K. Eckert<sup>1, 2, c)</sup>

<sup>1)</sup>*Institute of Process Engineering and Environmental Technology,  
Technische Universität Dresden, 01062 Dresden, Germany*

<sup>2)</sup>*Helmholtz-Zentrum Dresden-Rossendorf (HZDR), Institute of Fluid Dynamics,  
Bautzener Landstrasse 400, 01328 Dresden, Germany*

(Dated: 14 May 2020)

The deformation of the free surface of a paramagnetic liquid subjected to a non-uniform magnetic field has been studied. A transient deformation of the surface caused by the interplay of gravity, magnetic field and surface tension is observed when a permanent magnet is moved vertically downwards to the free surface of the liquid. Different concentrations of rare-earth metal salt ( $\text{DyCl}_3$ ) were used and different magnet velocities were studied. The deformation of the interface was followed optically by means of a microscope and recorded with a high-speed camera. The experimental results are compared and discussed with complementary numerical simulations. Detailed results are given for the static shape of the deformed surface and the temporal evolution of the surface deformation below the center of the magnet. The frequency of the surface oscillations is found to depend on the concentration of the salt and is compared with analytical findings. Finally, a potential application of the effects observed is presented.

**Keywords:** Magnetic field, magnetic gradient force, rare earth, dysprosium, interfacial instability, free surface, oscillations

---

<sup>a)</sup>Electronic mail: Barbara.Fritzsche@tu-dresden.de

<sup>b)</sup>Electronic mail: G.Mutschke@hzdr.de

<sup>c)</sup>Electronic mail: Kerstin.Eckert@tu-dresden.de

## I. INTRODUCTION

Magnetizable materials can be manipulated in an elegant way by means of the magnetic field gradient force. This so-called Kelvin force pulls paramagnetic material of positive magnetic susceptibility  $\chi$  into regions where the magnetic field has a higher magnitude. For a magnetic liquid, the force density can be written as:

$$\vec{f}_m = \frac{\chi_{\text{sol}}}{\mu_0} (\vec{B} \cdot \nabla) \vec{B} \quad (1)$$

where  $\mu_0$  and  $\vec{B}$  denote the vacuum permeability and the vector of the magnetic flux density.  $\chi_{\text{sol}}$  denotes the magnetic susceptibility of the solution which assembles from the product of the molar susceptibilities  $\chi_i^{\text{mol}}$  of the ions or molecules in solution and their concentrations  $c_i$ , i.e.

$$\chi_{\text{sol}} = \sum_i \chi_i^{\text{mol}} c_i + \chi_{\text{H}_2\text{O}} \quad (2)$$

For an aqueous paramagnetic salt solution, the susceptibility of the metal ion (e.g.  $\text{Dy}^{3+}$ ) dominates, and the diamagnetic susceptibility of water  $\chi_{\text{H}_2\text{O}}$  only weakly reduces the susceptibility of the solution<sup>1,2</sup>.

Paramagnetic ions have unpaired electrons, whose spin (an intrinsic magnetic moment of electrons) can be considered as like tiny magnets that tend to align with the vector of the magnetic field. Since the magnetic energy of ions is much smaller than the thermal energy of the solution, these ions are subject to Brownian motion and should not be influenced by the magnetic force. Surprisingly, robust changes in the concentration of paramagnetic ions under the presence of an inhomogeneous magnetic field were observed in earlier studies<sup>3-8</sup>. The manipulation of different fluids was studied; these contained both 3d ions<sup>4,5</sup>, such as  $\text{Cu}^{2+}$ ,  $\text{Mn}^{2+}$ ,  $\text{Fe}^{2+}$ , and 4f ions<sup>6-11</sup>, such as  $\text{Dy}^{3+}$ ,  $\text{Ho}^{3+}$ ,  $\text{Nd}^{3+}$  and  $\text{Gd}^{3+}$ . The origin of the magnetic properties is different for these metal ions. While in 4f ions the total angular momentum (orbital and spin) is important, in 3d ions a spin moment with only little or no orbital contribution characterizes the magnetic properties. Moreover, the unpaired magnetic 3d electrons are outermost and are strongly affected by the external magnetic field. Meanwhile, in the case of rare-earth ions, the magnetic 4f electrons are shielded by the electrons in  $5s^2$  and  $5p^6$  shells and are less strongly affected. Therefore, the magnetic properties of rare earths are stable in the external magnetic field and the rare earth magnets are much harder

to demagnetize. The motion of paramagnetic metal ions was also studied on and inside gel structures exposed to an inhomogeneous magnetic field<sup>3,7,12–14</sup>.

The physical mechanism of the magnetic separation of rare earth ions in two works<sup>4,6</sup> was explained in recent studies<sup>9,11</sup>. The evaporation of the solvent provides a concentration gradient at the liquid’s free surface. The magnetic gradient force stabilizes regions with higher concentrations and enables the levitation of the enriched layer over the less dense bulk solution. Hence, a key element of this process is the existence of a free liquid-gas interface. However, a non-uniform magnetic field not only modifies the transport process in the paramagnetic liquid but also affects the stability of this interface. The main motivation behind this work is to gain a better understanding of the behavior of the free surface of a paramagnetic solution in an inhomogeneous field, which is a precondition for designing a magnetic separator for rare earth elements.

Generally, magnetic fluids adapt the morphology of their surface in magnetic fields to minimize its energy. The resulting interfacial instabilities in super-paramagnetic liquids, e.g ferrofluids ( $\chi_{\text{FF}} = 0.4 - 3.7^{15}$ ) under external magnetic fields have been studied intensively in recent decades. The best known instability is the normal-field or Rosensweig instability<sup>16</sup>. It appears when a ferrofluid (magnetic fluid) is subjected to a sufficiently strong vertical uniform magnetic field. The surface generates an ordered pattern of peaks and valleys. The dynamics of a single peak of the Rosensweig instability were studied in<sup>17,18</sup>. Experimental studies under micro-gravity showed that a sort of normal-field instability even forms if the magnetic field is applied parallel to the fluid surface<sup>19</sup>. Recently, a modified normal-field instability in ferrofluids in the presence of a magnetic field gradient was reported<sup>20</sup>. For a thin layer of ferrofluid, the impact of the field gradient on the critical magnetization above which the instability appears, and the characteristic wavelength, have been identified. It was found that the magnetic field gradient force stabilizes the interface, hence a higher magnetic force is needed for the onset of instability.

By contrast, much less is known about the related surface instabilities of paramagnetic solutions. While the surface profile between aqueous copper sulfate solution and water was insensitive to the direction of a high magnetic field (10 T)<sup>21</sup>, experiments with liquid oxygen ( $\chi_{\text{LOX}} = 3.47 \cdot 10^{-3}$ ) in an inhomogeneous magnetic field<sup>22</sup> showed similar findings to the surfaces of ferrofluids<sup>20</sup>. Paramagnetic liquids exposed to magnetic fields can further be used to control the mixing behavior of liquids in tubes, as was shown in<sup>23</sup>.

By means of a combination of experiments and numerical simulations, here, for the first time, we analyze the behavior of the free surface of a paramagnetic liquid after it moves into an inhomogeneous magnetic field. We demonstrate that the response consists of the superposition of damped surface oscillations onto a static deformation. Based on the excellent agreement between experiments and simulations in terms of frequencies and surface shape, we can clearly identify the origin of the surface oscillations. These are gravity-driven standing waves with an effective gravitational acceleration modified by the magnetic field gradient, and which can be approximated by Bessel functions of zeroth order. Finally, an application of the phenomena studied is provided in the form of a thermal/electric switch employing  $\text{DyCl}_3$  solutions.

## II. THEORY

Bringing a permanent magnet closer to the surface of a paramagnetic liquid will cause a transient deformation of the shape of the surface and a flow inside the liquid. The velocity  $\vec{u}$  in the liquid is given by solving the Navier-Stokes equation for an incompressible fluid under the influence of gravity, magnetic force and surface tension, complemented by the incompressibility constraint:

$$\rho \left( \frac{\partial \vec{u}}{\partial t} + (\vec{u} \cdot \nabla) \vec{u} \right) = -\nabla p + \eta \Delta \vec{u} + \rho \vec{g} + \vec{f}_m, \quad (3)$$

$$\nabla \cdot \vec{u} = 0 \quad (4)$$

Here,  $\rho$ ,  $\eta$ ,  $t$ ,  $p$  and  $\vec{g}$  denote the density and the dynamic viscosity of the liquid, time, pressure and the vector of gravitational acceleration, respectively. Eq. 3 has to be complemented by proper boundary conditions. At the free surface of unknown shape, as well as capillary stress, Maxwell stress also had to be considered.

Under the assumption of a current-free magnetic field  $\nabla \times \vec{H} = 0$ , collinear magnetization of the liquid  $\vec{M} = \chi_{sol} \vec{H}$  and an isothermal and irrotational flow field  $\nabla \times \vec{u} = 0$ , a ferrohydromagnetic Bernoulli equation can be derived<sup>24</sup>,

$$p - \frac{\chi}{2\mu_0} B^2 + \frac{\rho}{2} u^2 + \rho gh = \text{const.}, \quad (5)$$

where  $B$  denotes the magnitude of the magnetic flux density. From this equation it can be seen that the magnetic pressure (second term) might counteract gravity, thus tending

to elevate the surface of a magnetic liquid. When a fluid at rest in a constant horizontal magnetic field is considered, the height difference  $\Delta h$  can be calculated as amounting to

$$\Delta h = \frac{\chi}{2\mu_0} \frac{B^2}{\rho g} \quad (6)$$

which is known from Quincke's method for determining the magnetic susceptibility of a liquid. When a constant vertical magnetic field is considered, a further term arises in this equation from the normal Maxwell stress at the interface, and the relation reads<sup>24</sup>:

$$\Delta h = \frac{\chi}{2\mu_0} \frac{B^2}{\rho g} (1 + \chi) \quad (7)$$

For paramagnetic salts dissolved in water, however, the correction compared to Eq. 6 is small, since  $\chi_{sol} \ll 1$ .

To derive the last two equations, the surface was assumed to be flat. However, when the liquid is exposed to a spatially inhomogeneous magnetic field caused e.g. by a small permanent magnet placed above the surface of a large reservoir, the surface deformation will depend on the lateral coordinate. Therefore, the capillary pressure  $\Delta p_c$ ,

$$\Delta p_c = \frac{\sigma}{2R}, \quad (8)$$

comes into play. Depending on the surface curvature  $1/R$ , this tends to reduce the height difference. Here,  $\sigma$  denotes the surface tension between the liquid and the air. Axial symmetry regarding the chosen magnet configuration was assumed.

In the general case of an inhomogeneous magnetic field above a free surface of a magnetic liquid, the shape of the free surface of a liquid at rest follows from Eq. (3). In detail, it is determined by the solution of the following equation along the interface<sup>24</sup>:

$$-\nabla p = \rho \vec{g} + \mu_0 M \nabla H; \quad p = p_0 - \frac{2\sigma}{R} - \frac{\mu_0}{2} M_n^2 \quad (9)$$

where  $M_n$  denotes the interface-normal component of the magnetization. Again, axial symmetry was assumed. In general, these equations need to be solved numerically, as analytical solutions can only be found for specific generic geometries<sup>25</sup>. The application of a magnetic field to a fluid at rest usually leads to a transient response by the liquid. If a free surface exists, surface waves are generated. Purely hydrodynamic surface waves, generated e.g. by mechanical or acoustic actuation, are determined by the influence of both gravity (acceleration  $g$ ) and surface tension ( $\sigma$ ). The dispersion relation for the angular frequency  $\omega = 2\pi f$

is given by<sup>26</sup>:

$$\omega^2 = gk + \frac{\sigma}{\rho}k^3 \quad (10)$$

Here,  $k = 2\pi/\lambda$  and  $\lambda$  denote the wave number and the wavelength of the wave mode under consideration. Expression (10) is valid if the wavelength does not considerably exceed the height of the vessel (“deep water”), a constraint which is fulfilled in the case under consideration here (see Section VI). Furthermore, viscous effects have been neglected so far, and will be discussed later in Section VI.

For surface waves of magnetic liquids in an inhomogeneous magnetic field, Eq. (10) has to be modified and also extended and reads as<sup>22,24,27</sup>

$$\omega^2 = g_{\text{eff}}k + \frac{\sigma}{\rho}k^3 - \frac{\chi_{\text{sol}}^2}{4\rho} \frac{B_0^2}{\mu_0} k^2, \quad (11)$$

where  $B_0$  denotes the magnitude of the magnetic flux density at the surface. The magnetic pressure caused by an inhomogeneous magnetic field can be understood as modifying the gravitational acceleration, and the resulting effective value  $g_{\text{eff}}$  is given by:

$$g_{\text{eff}} = g - \frac{\mu_0 M}{\rho} \cdot \frac{\partial H}{\partial z} \quad (12)$$

where the vertical coordinate  $z$  points in an upward direction. The role of  $g_{\text{eff}}$  is discussed in more detail in Section VI. The additional term arising in Eq. (11) can usually be neglected for aqueous solutions containing paramagnetic ions, since, as already mentioned above,  $\chi_{\text{sol}} \ll 1$ .

### III. EXPERIMENTAL SETUP

Paramagnetic solutions of the rare earth salt Dy(III) chloride hexahydrate,  $\text{DyCl}_3 \cdot 6 \text{H}_2\text{O}$  (99.9%, abcr GmbH & Co. KG) were prepared by dissolving the salt in 0.1 M of hydrochloric acid. Four different concentrations  $c_0$  (0.25 M, 0.5 M, 0.75 M and 1 M; 1 M = 1 mol/l) of  $\text{DyCl}_3$  were considered. The saturation concentration of  $\text{DyCl}_3$  in water is approx. 3.5 M - 3.8 M<sup>28</sup>. Thus, by choosing 0.1 M hydrochloric acid and concentrations considerably below the saturation concentration, a complete dissociation of the dysprosium salt without precipitation in the solution was ensured.

$\text{DyCl}_3$  solution was injected into an optical cuvette with a square cross section  $D \times D$  ( $D = 60$  mm) and a height  $H = 20$  mm, see Fig. 1-a. The same filling protocol was applied during all experiments, which were performed at room temperature of  $22.7^\circ\text{C} \pm$

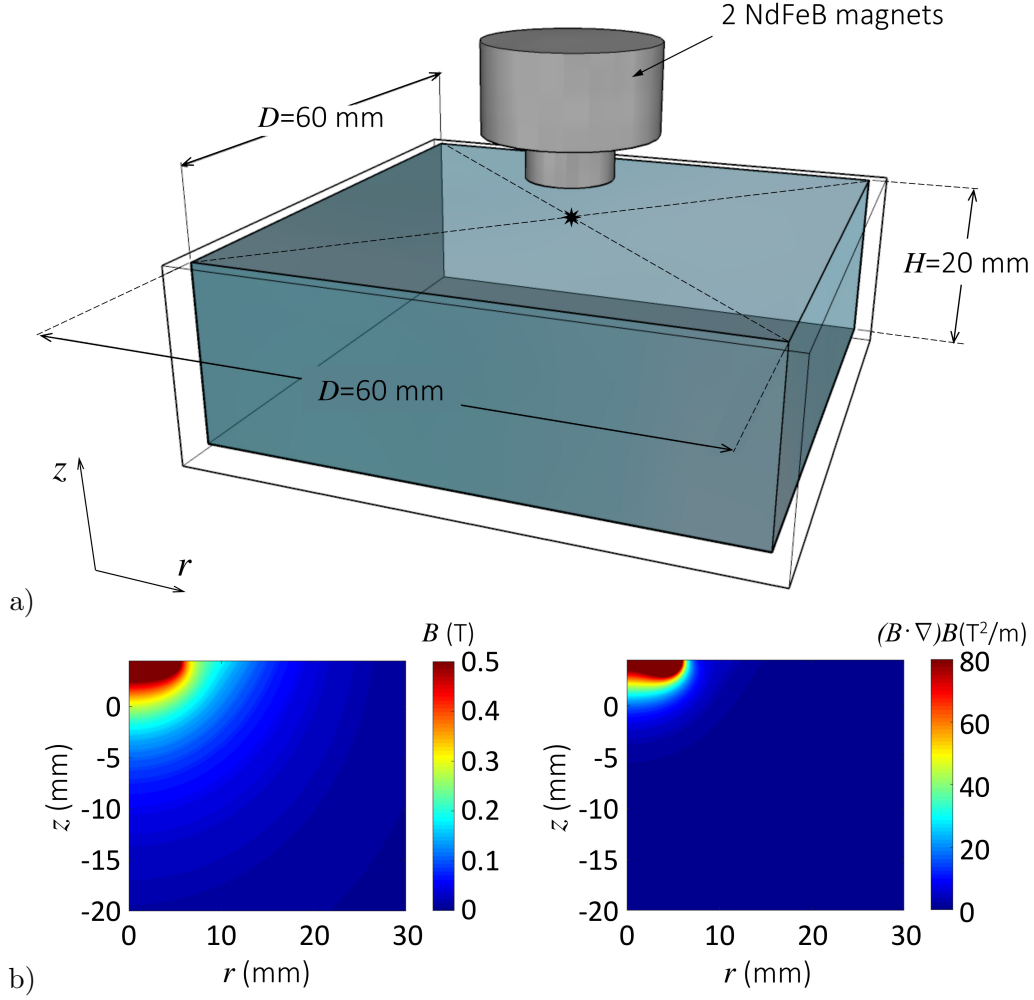


FIG. 1. (a) Sketch of the experimental setup. The transparent glass cuvette contains the para-magnetic  $\text{DyCl}_3$  solution. The origin of the cylindrical coordinate system is marked by a star. The direction of gravity and the magnet's approach are along the  $-z$  direction. (b) Magnetic flux density and the magnetic field gradient term  $|(\vec{B} \cdot \nabla)\vec{B}|$  for the lowest magnet position at  $z_0 = 4.5$  mm (simulation result). The maximum values of both quantities shown were limited to enhance the presentation.

0.4 °C. The magnetic field was provided by an axial assembly of two cylindrical NdFeB magnets of different sizes: a large one (radius = height = 10 mm) on top and a smaller one (radius = height = 5 mm) below (see Fig. 1-a). Both magnets are magnetized in the upward direction. In the following, this magnet assembly is referred to as *magnet* for simplicity. The magnetic flux density  $B$  and the magnetic field gradient term  $|(\vec{B} \cdot \nabla)\vec{B}|$  calculated



by finite-element simulations (see Section IV) are shown in Fig. 1-b for the lowest magnet position considered, where the lower magnet surface is placed at  $z_0 = 4.5$  mm. The magnet was precisely located above the center of the cuvette. It was moved vertically along the symmetry axis of the cuvette in  $z$  direction, see Fig. 1-a) using a motorized translation stage (Newport). The diameter of the magnet was chosen to be considerably smaller than the width  $D$  of the cuvette to limit the magnetic interaction with the center part of the cuvette. Thus, possible sloshing phenomena related to the motion of the contact line of the liquid along the side walls are reduced.

At the beginning of the experiments, the bottom of the magnet was 20 mm above the surface of the liquid ( $z = 20$  mm). The magnet was then moved vertically downwards by 15.5 mm ( $z_0 = 4.5$  mm) towards the free surface, where it stayed for 5 s. After this time, the magnet was removed upwards to its initial position with the same velocity. Both final positions of the magnet were kept constant through all the experiments. Two different velocities of the magnet were investigated, which can be grouped into a *slow case* (0.5 mm/s) and a *fast case* (20 mm/s). All the experiments were repeated three times.

The interfacial deformation was monitored using a microscope connected to a high-speed camera (IDT NX4-S1), and applying a background illumination provided by a LED and a diffuser. The measurements were carried out at a magnification of  $M = 5$  (resolution of 210 pixels/mm) and a frame rate of 200 images/s.

Fig. 2 shows characteristic stages of the interface in the center of the cell. The left image depicts the undisturbed flat surface prior to magnetic actuation (height position  $h_0$ ). The subsequent two pictures show snapshots of the deformed surface. The timescale is defined such that at  $t = 0$  s (Fig. 2, center) the magnet has reached the final position, closest to the interface. The right-hand image presents the static deformation after the oscillations were damped out.

To reconstruct the entire surface of the liquid at a given field of view of 4.8 mm, a technique explained in Section V A was applied. For the detailed study of the surface of the liquid, the latter was additionally identified using spherical polystyrene particles (diameter of 36  $\mu\text{m}$ ) to ensure a better contrast, see Fig. 3.

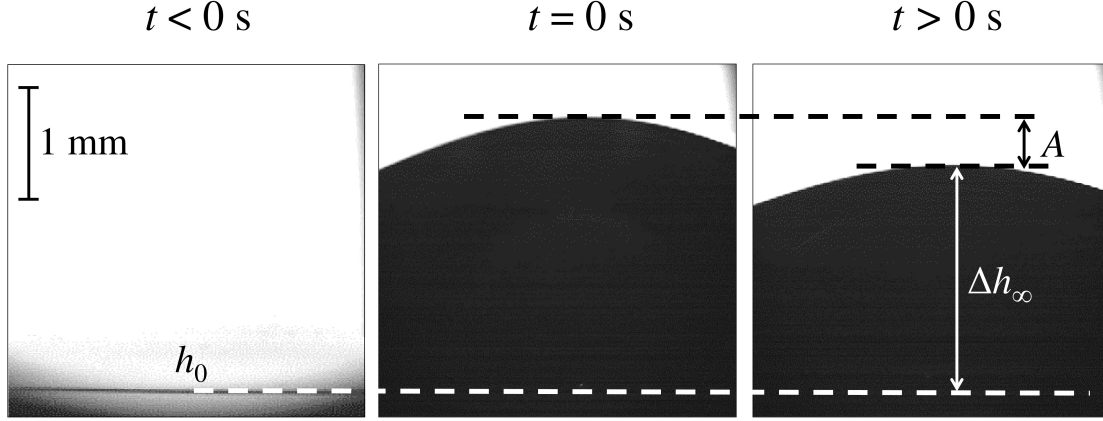


FIG. 2. Zoomed view of the surface of a  $\text{DyCl}_3$  solution and its deformation under the influence of a magnetic field near the cell center. Left: Flat surface (vertical position  $h_0$ ) when the magnet is far away. Center: Deformed surface when the magnet has reached the closest position ( $t = 0$ ). The point in the center (marked by a star) is denoted as  $h(t = 0, r = 0)$ . Right: Deformed surface at a later point in time  $t > 0$  s. The marked distances refer to Eq. 15.

#### IV. SIMULATION SETUP

Numerical simulations were performed to calculate the transient deformation of the surface of the liquid and to compare the data with the experimental results. The following geometrical simplifications and modifications were applied. As the diameters of the cylindrical NdFeB magnets above the center are small compared to the diameter of the vessel, a cylindrical vessel of diameter 60 mm was considered. Thus, because of axial symmetry, 2D simulations were performed in the  $(r, z)$  plane. The transient simulations start with a plane surface above which the magnet is located in the final position of the experiment, i.e. 4.5 mm above the surface. Compared to the finite speed at which the magnet approaches the surface in the experiments, this corresponds to an infinitely fast approach, and will thus lead to larger oscillation amplitudes of the surface compared to the experiment, even in the case of the fast approach in the experiment. The simulations were performed using the commercial finite-element multiphysics software COMSOL V.52a.

The magnetostatic problem to calculate the magnetic field of the two permanent magnets is performed as a preprocessing step. This is possible since the magnetic field does not change over time and space because the magnetization of the solution is low compared to

TABLE I. Material parameters of pure water and of the different aqueous  $\text{DyCl}_3$ -solutions used in the simulations and calculations in Table II (from<sup>6,31</sup>).

$c$ [M]	$\rho$ [kg/m <sup>3</sup> ]	$\eta$ [Pa·s]	$\chi_{\text{sol}}$
0.0	997.0	$1.0 \cdot 10^{-3}$	$-9.10 \cdot 10^{-6}$
0.25	1060.0	$1.112 \cdot 10^{-3}$	$1.28 \cdot 10^{-4}$
0.5	1118.5	$1.224 \cdot 10^{-3}$	$2.67 \cdot 10^{-4}$
0.75	1180.3	$1.461 \cdot 10^{-3}$	$4.04 \cdot 10^{-4}$
1.0	1239.3	$1.724 \cdot 10^{-3}$	$5.41 \cdot 10^{-4}$

the external field strength. In order to avoid any influence from boundary conditions applied at a finite distance from the setup, infinite elements were used at the outer edges.

The simulation solves the Navier-Stokes equation (Eq. 3) for the paramagnetic liquid. This includes the gravity force and the magnetic gradient force (Eq. 1) based on the magnetic susceptibility of the solution and the distribution of the magnetic field and its gradient as calculated previously. The deformable interface between the air and the salt solution is taken into account using the Arbitrary Lagrangian Eulerian Method as described in<sup>29,30</sup>. The boundary conditions applied are a no-slip condition at the walls of the vessel and a free-slip condition at the surface, with a fixed contact point at the brim. The material parameters of density, viscosity and magnetic susceptibility of the different aqueous  $\text{DyCl}_3$ -solutions are listed in Table I. For the surface tension, the value  $\sigma = 0.0718 \text{ N/m}$  of a water-air interface was used. Finally, an unstructured grid of about 113,000 elements was used for the simulations resulting from validation studies in order to properly resolve regions where large gradients occur or the surface is moving. For the case of a 0.75 M  $\text{DyCl}_3$  solution, which is the maximum concentration investigated numerically, the magnetic force was linearly increased within an initial period of 1 s in order to reduce the initial amplitude of the surface deformations (see Section V B).

## V. RESULTS

The initially flat surface of the  $\text{DyCl}_3$  solution,  $h(r, t)$ , becomes unstable when exposed to an inhomogeneous magnetic field. This surface deformation proceeds in two steps: an initial

oscillatory phase which evolves into a stationary deformation after the oscillations have been damped out. In the following, the surface deformation  $\Delta h(r, t)$  due to the magnetic field is related to the initial level of the interface,  $h_0(r)$  without field (cf. Fig. 2), given by

$$\Delta h(r, t) = h(r, t) - h_0(r). \quad (13)$$

The unusual feature of a lateral dependence of the undisturbed surface height  $h_0(r)$  is introduced to account for possible evaporation effects which may take place during the measurements, as explained below in detail.

### A. Stationary shape of the free surface

We first focus on investigating the stationary surface deformation  $\Delta h_\infty(r)$  that remains after the oscillations have declined. Figs. 3 and 4 show the surface topology of a 0.75 M solution between the center and the edge of the cell without any influence from the magnetic field (Fig. 3-a) and 4 s after the magnet has reached its final lower position in the case of a fast approach (Fig. 3-b). Considering the axial symmetry of the setup in the center region of the cuvette, only one half of a cuvette was studied, i.e.  $0 \text{ mm} < r < 30 \text{ mm}$ .

To capture the whole free surface at a given field of view of 4.8 mm in this interval, a series of 9 consecutive measurements were necessary, at different lateral positions of the camera with slightly overlapping regions. Each measurement of the temporal response of a surface segment on the approaching magnet takes about 5 min, after which adjustments are necessary to change the field of view. Thus, in total, the measurements take about two hours. During this long time, a small amount of solvent evaporates, which is visible as a small depression in Fig. 3-a. The amount of evaporated solvent was estimated to be  $0.8 \text{ cm}^3$ , which represents less than 1.1% of the solution volume in total. Correspondingly, the change in the bulk concentration due to evaporation also remains negligible. Thus, segment by segment, the undisturbed surface positions  $h_0(r)$  and the deformed surface positions  $h(r, t)$  were measured.

The quantitative data extracted in these segments from the position of the polystyrene particles in Fig. 3-b are shown in Fig. 4-a. The blue dots represent the center of the particles. Only moderate image processing was performed and not all particles which are out of focus were removed, which contributes to the fluctuations in the data. The data were fitted using

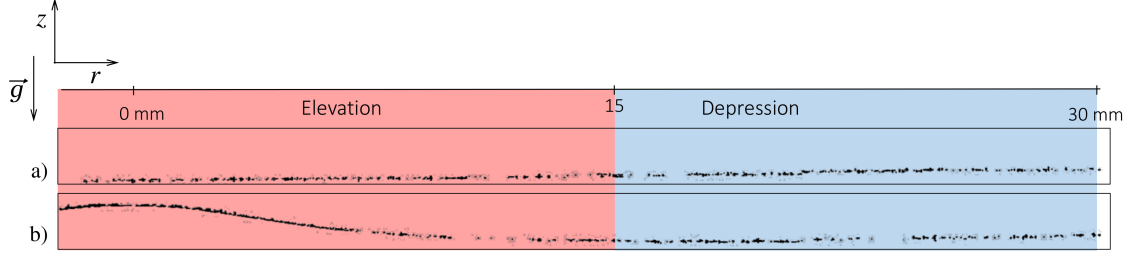


FIG. 3. Interface structure of the 0.75 M  $\text{DyCl}_3$  solution, shown at an aspect ratio of  $z : r = 1 : 1$  (a) without magnetic field influence, (b) 4 s after the magnet reached its end position (fast case). The interface is identified using monodisperse polystyrene particles (darker points in the picture), which rest on the liquid's surface. The figure represents the interface in the central plane of the cuvette. The edge of the cuvette is on the right-hand side of the figure ( $r = 30$  mm), while the center of the magnet is on the left side of the figure ( $r = 0$  mm), where the largest elevation of fluid is seen.

a polynomial of the seventh degree in order to obtain a smooth curve. This curve is plotted in Fig. 4-b together with the static surface deformation for other Dy(III) concentrations, obtained by simulations.

The elevation reaches a maximum in the center of the cell, vertically below the magnet ( $r = 0$  mm). As a result of mass conservation, there is a surface depression at the outer part ( $r > 15$  mm). The static shapes of the surface as obtained from the experiment and simulation for the 0.75 M solution correspond very well. The maximum elevation of the simulation result is slightly larger than the measured value, and the radial position of zero height is found at a slightly smaller radial position than the measured value. Both these small deviations may result from a moving contact point at the outer wall, which cannot be avoided in the experiment, and is visible when looking at  $r = 30$  mm. In general, as seen from the simulation results, higher concentrations lead to higher surface elevations in the center, compared to which other changes in the surface shape are small. The radial position of zero height difference moves slightly towards the center of the cell when the concentration increases (at 13.8 mm for 0.25 M, at 12.3 mm for 0.75 M).

Fig. 5 summarizes the behavior of the stationary elevation at the center of the cell  $\Delta h_\infty(r = 0)$  at different  $\text{Dy}^{3+}$  concentrations. There is very good agreement between the experimental results and the simulations for  $\Delta h_\infty$ . As already seen in Fig. 4-b, the higher

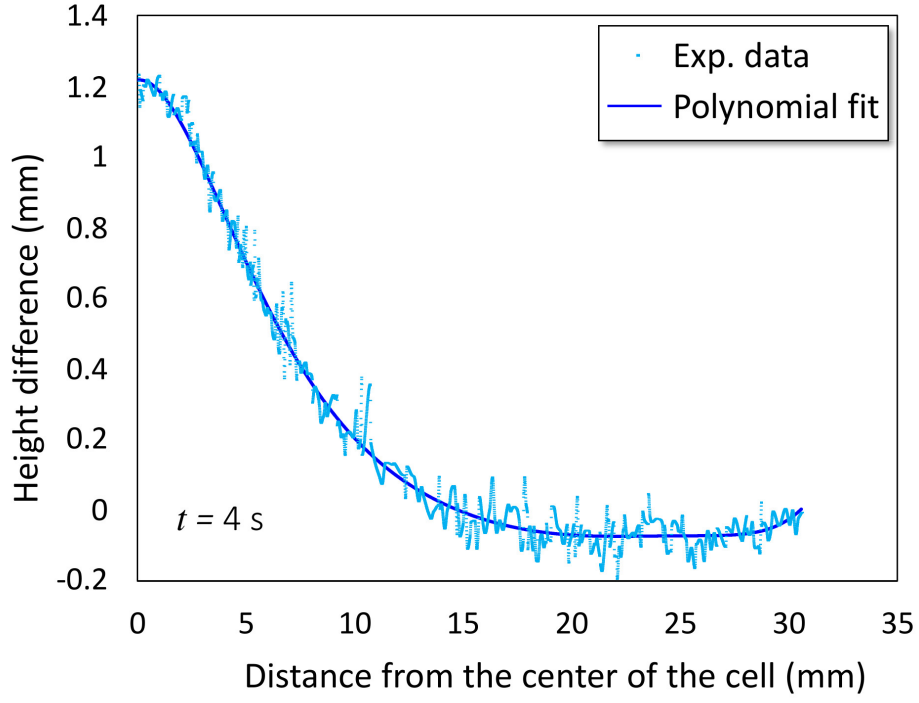
the salt concentration, i.e. the magnetic susceptibility of the solution, the higher the elevation of the interface at  $r = 0$ . For the magnet assembly studied here, the relation appears to be nearly linear for concentrations larger than 0.25 M.

## B. Temporal evolution of surface height

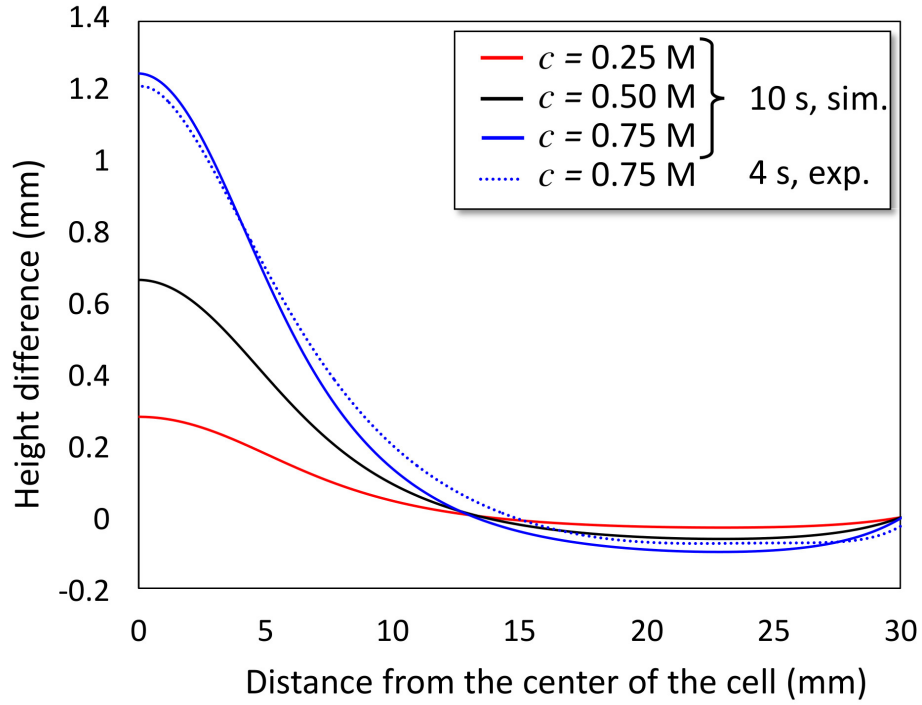
As already mentioned before, the approaching magnet causes an oscillatory response by the surface of the paramagnetic liquid. To analyze this oscillatory behavior, we study the development of the height difference  $\Delta h(r = 0, t)$  in the center of the cell where  $\Delta h(r, t)$  attains its maximum. Fig. 6 shows the experimental results of the  $\Delta h(t)$  dynamics for different concentrations at both limiting cases: the slow case (Fig. 6-a) and the fast case (Fig. 6-b). The time axis is defined such that at  $t = 0$  s the magnet has reached its final position close to the surface. As can be seen for  $t < 0$  s, during the approach of the magnet, the surface is rising, whereby its rising speed depends on the approach velocity of the magnet. For  $t \geq 0$ , both cases display sinusoidal interface oscillations, the amplitude of which is being damped with time. As expected, the initial amplitude of the oscillations is larger the larger the concentration is.

The oscillations in general result from the interplay between the inertia of the liquid, which is accelerated by the field gradient force on the one hand, and gravity and surface tension on the other hand, which aim to flatten the disturbance. Due to inertia, the liquid with its free surface is not able to adapt fast enough to the increasing magnetic forcing caused by the approaching magnet. Thus, after the magnet has reached the final position, an overshooting is observed. This results in larger amplitude  $A$  (see Fig. 2) for the fast cases (Fig. 6-b) than for the slow cases (Fig. 6-a). After about 5 s, the oscillations are essentially declined in all cases and the static height differences correspond to the values already discussed in the subsection above. Slightly later, the magnet is removed, which causes the height difference to relax.

Fig. 7 shows the results of the simulation as a comparison. While they are very similar to the experiments in the second half of the simulated timespan, a slightly different behavior can be observed in the first phase. The reason is that, due to the details of the simulation described above, the initially flat surface is abruptly exposed to the action of the magnet at  $t = 0$ , which corresponds to an infinite speed of approach in terms of the experiment.



a)



b)

FIG. 4. Shape of the static surface deformation after the decay of oscillations: a) experimental result for 0.75 M  $\text{DyCl}_3$  observed at 4 s after the fast approach of the magnet, b) numerical results for different bulk concentrations of  $\text{DyCl}_3$  in comparison with the experimental result for the 0.75 M solution (fitted curve).

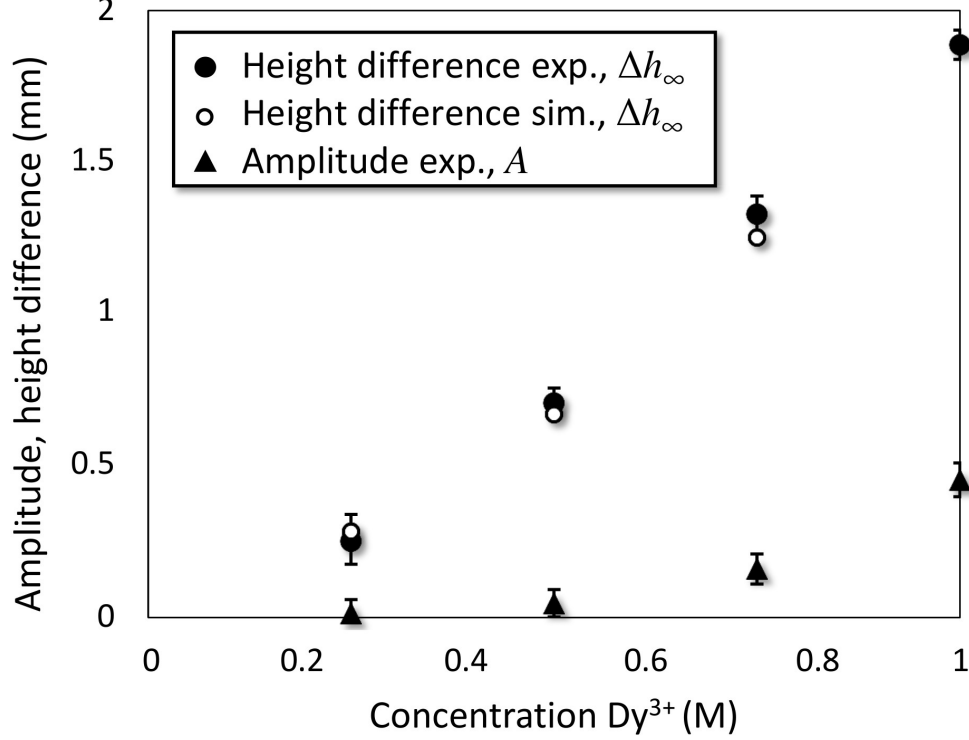
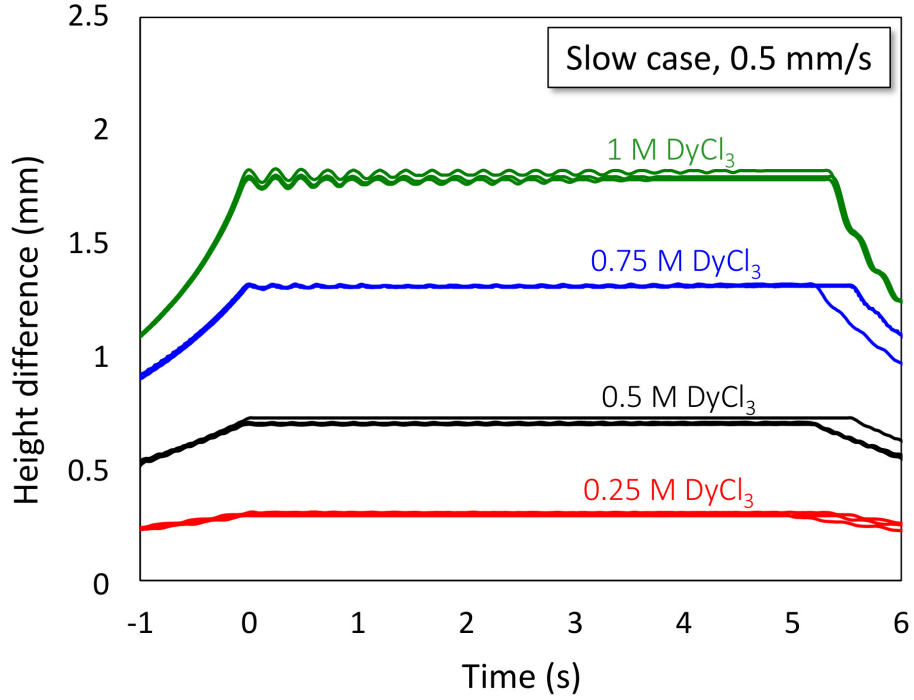


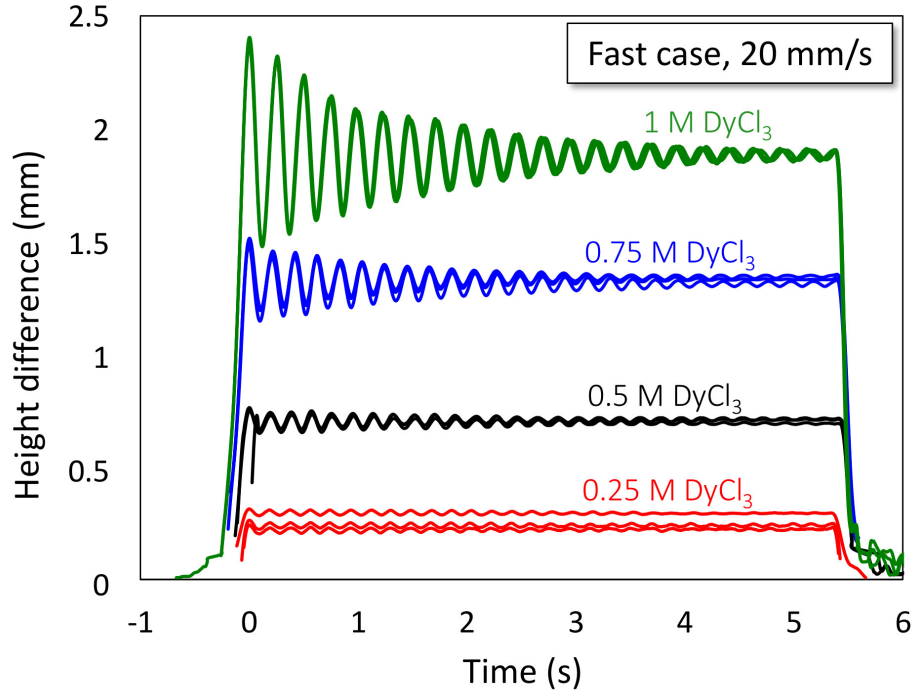
FIG. 5. Static surface elevation,  $\Delta h_\infty$ , below the center of the magnet after decay of oscillation versus bulk concentration: comparison between experimental and numerical results. The error bars represent the minimum and maximum value of experimental results. Additionally, the fitted value of the initial amplitude  $A_1$  of the transient oscillations according to Eq. 15 is given for the fast application of the magnet (see Section V B).

This results in considerably larger initial amplitudes  $A$  when compared even to the fast experimental case. For this reason, the case of 0.75 M had to be treated differently in the simulation. To mimic an approaching magnet, the magnitude of the magnetic force  $f_m$  was linearly increased over a period of 1 s. As can be seen, the initial amplitude of oscillation is strongly reduced. A further difference due to the infinitely fast application of the magnet in the two simulation cases of 0.25 M and 0.5 M becomes visible in the initial time interval  $0 < t < 6$  s, where different dynamics are observed. From the temporal behavior of the height difference it becomes obvious that more than one single frequency is involved in the oscillations, which seems not to be the case for the experimental results. Moreover, for these two cases, the first maximum surface elevation is reached with a slight delay ( $t > 0$  s) in comparison with all the experimental cases and also the simulated case of 0.75 M, where





a)



b)

FIG. 6. Experimental result of the interfacial dynamics in the center of the cell for all investigated  $\text{DyCl}_3$  concentrations for the slow (a) and the fast (b) case. The magnet velocity is given in the insert. At  $t = 0$ , the magnet has reached the final position near the surface. At  $t = 5$  s, the magnet is removed upwards again.

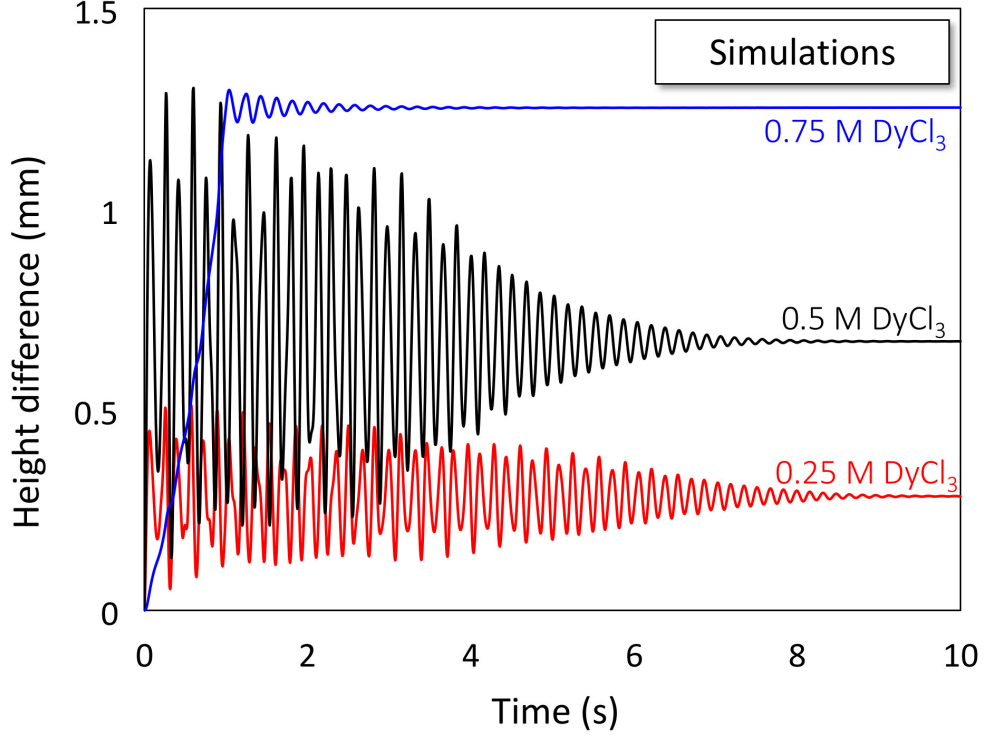


FIG. 7. Simulated interfacial dynamics in the center of the cell for different  $\text{DyCl}_3$  concentrations.

the maximum is reached at  $t = 0$  s. Finally, for later points in time,  $t > 6$  s, only a single oscillation frequency remains in these two simulation cases, in qualitative agreement with all the experimental results and also the special simulation case of 0.75 M as discussed above.

The oscillation frequencies extracted from Figs. 6 and 7 are plotted in Fig. 8 for the different  $\text{Dy}^{3+}$  ion concentrations. As is clearly visible from the experiment, the frequency decreases with an increasing concentration. The simulation results reproduce this trend very well, despite a minor offset of about 12% towards larger frequencies. This offset may be due to the fact that the contact line at the outer wall of the cuvette, which is full to the brim, cannot be completely prevented from moving in the experiment; it is well known that this slightly reduces the oscillation frequency of the surface waves<sup>32</sup>.

To better understand the nature of the surface oscillations which are excited, we compare them with mechanically triggered waves. For that purpose, a small water droplet produced by a 1 mL syringe falls from the tip of the needle to the center of the cuvette, which is filled with pure water. The height of the free fall is 40 mm. The dynamics of the water surface at the center after excitation by the drop, which reaches the surface at  $t = 0$  s, is shown in

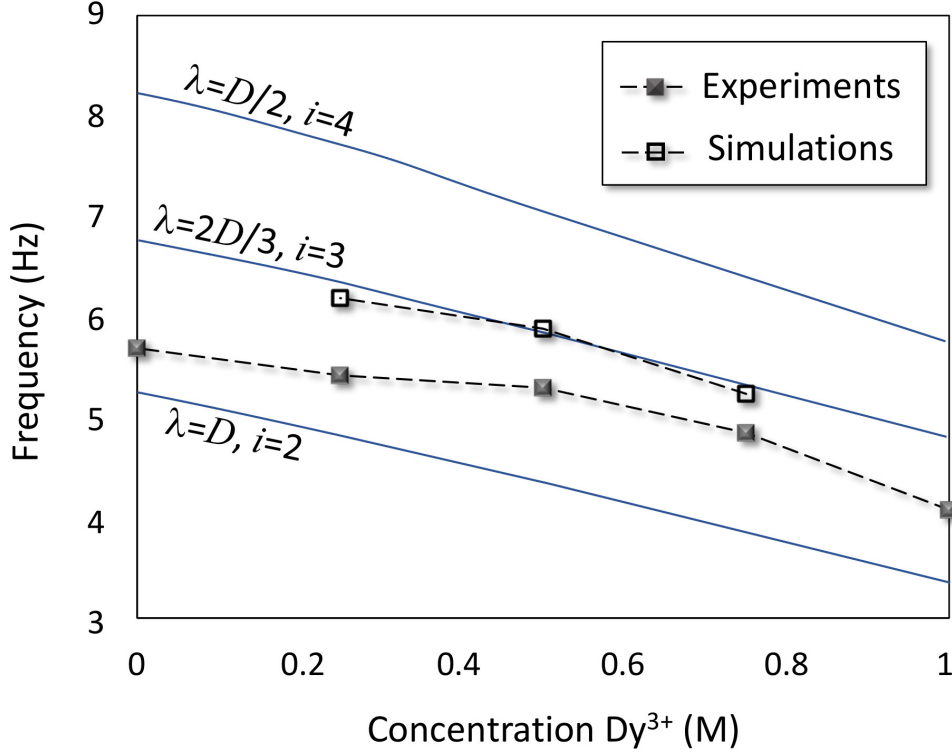


FIG. 8. Frequency of the surface deformation versus bulk concentration: comparison between experiments and simulations. The solid lines represent predicted frequencies of different modes of surface waves as discussed later in Section VI.

Fig. 9. Similarly to the two simulated cases discussed above, for short times after the drop's impact, surface oscillations of different frequencies are visible as non-monotonic variations in the oscillation amplitude. After about 3 s, sinusoidal oscillations of a single frequency  $f = 5.7$  Hz and a monotonically decaying amplitude remain. This point fits nicely into the frequency trend plotted in Fig. 8, where it is inserted for  $c_{\text{Dy(III)}} = 0$  M. As the volume of the drop is very small ( $\approx 9 \mu\text{L}$ ) compared to the volume of the cuvette ( $= 0.072$  L), no static height difference remains in Fig. 9.

## VI. DISCUSSION

When a permanent magnet quickly approaches the free surface of a paramagnetic liquid, beside a static deformation of the surface shape, surface oscillations are triggered. These oscillations are standing waves, as the contact line is nearly perfectly pinned at the side

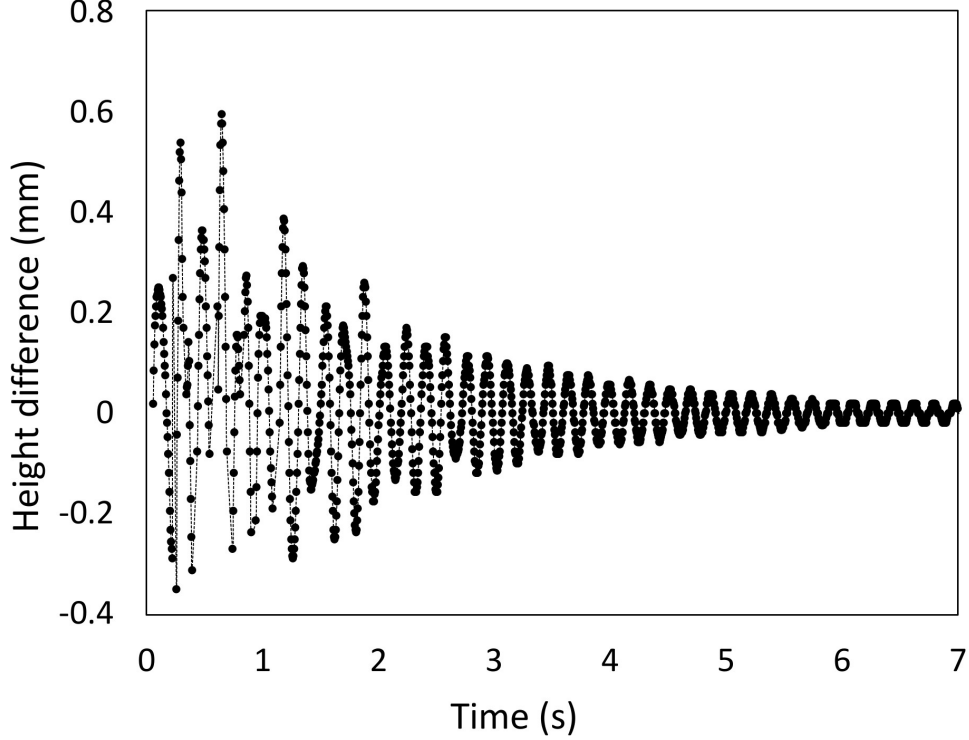


FIG. 9. Dynamics of the surface of water in the cuvette excited by a falling drop. At  $t = 0$  s the drop reaches the surface.

walls of the cuvette, which is full to the brim. Once excited, the oscillations are damped naturally with time because of viscous friction in the bulk, surface tension, and friction at the contact line<sup>32</sup>.

In the following, we restrict our focus to axisymmetric surface deformations, which can be described as the sum of the asymptotic surface shape  $A_0(r)$  and a series of radial eigenfunctions  $F_i(r)$  which oscillate over time but also decay over time<sup>32,33</sup>:

$$\Delta h(r, t) = A_0(r) + \sum_{i=1}^{\infty} A_i \cos(2\pi f_i t + \delta_i) F_i(r) e^{-\gamma_i t}. \quad (14)$$

Here,  $R$ ,  $A_i$ ,  $f_i$ ,  $\delta_i$  and  $\gamma_i$  denote the radius of the vessel, the amplitude, the frequency, the phase shift and the damping factor of mode  $i$ , respectively.

The shape of the static deformation  $A_0(r)$  was studied in Section V A and is strongly influenced by the width of the magnet, which in the case considered here is much smaller than the width of the cuvette  $D = 2 \cdot R$ . As a result, the surface is elevated beneath the

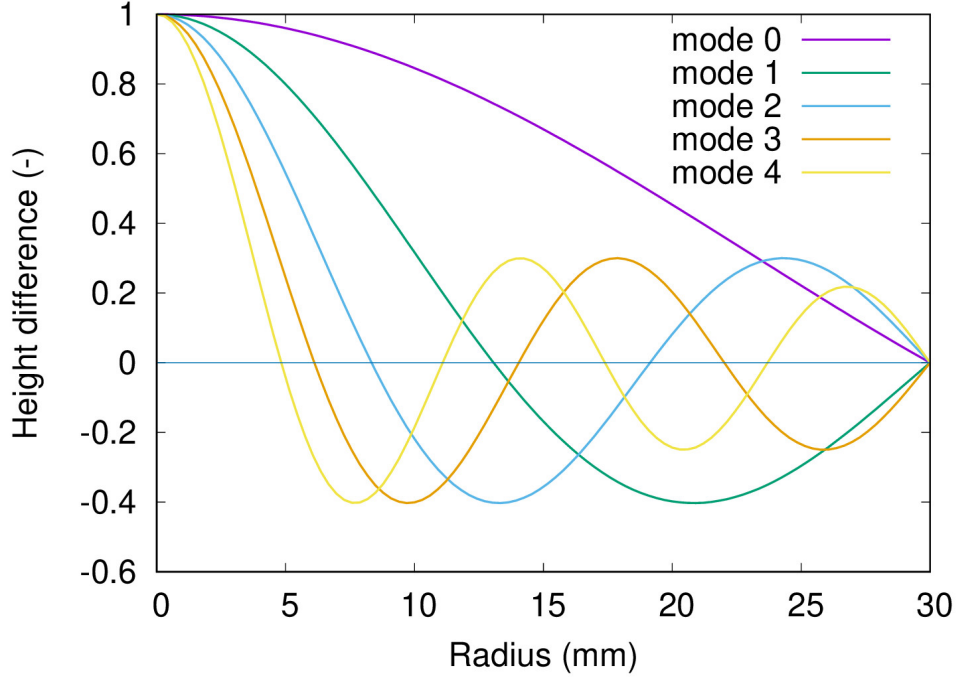


FIG. 10.  $N$  Modes  $i = 0$  to  $i = 4$  of a Bessel function expansion, which are radial eigenmodes of the oscillating membrane of a drum.

magnet only, and, due to volume conservation, slightly lowered in the outer part. Therefore, a zero must occur, which is found from the simulations at about  $r \sim 13$  mm for all the salt concentrations investigated (see Fig. 4), in good agreement with the experimental value measured for  $c = 0.75$  M.

Beside the static deformation, the oscillations caused by the fast approach of the magnet may be understood similarly to ordinary gravity-capillary waves, for which the dispersion relation derived for infinite domains is shown in Eq. (10). Taking the magnetic field into account then leads to the modified dispersion relation (11), where the gravitational acceleration at the static surface has to be updated in line with Eq. (12). We have to admit that, for further reasons, Eq. (11) may only hold true approximately, as in our case the gravitational acceleration is only altered locally beneath the magnet. Thus, in our case,  $g_{\text{eff}}$  depends on  $r$  and the vertical coordinate  $z$ .

For a cuvette of a given diameter, the eigenmodes, their wave numbers and frequencies result from solving a related eigenvalue problem where the depth of the cuvette also needs to be considered (e.g. see<sup>32,33</sup>). We do not intend to go into more detail here, but instead, for illustration only, show in Fig. 10 the radial eigenmodes of a drum membrane excited by

actuation in the center<sup>34</sup>, offering a qualitative insight into what the axisymmetric modes look like. The aspect we would like to point out is that these modes are characterized by a growing number of nodes. The eigenmodes shown in Fig. 10 are the Bessel functions of index zero, the argument of which is stretched such that the nodes match with the pinned contact line at the outer wall. Hence, the functions are given as  $J_0(x_i r/R)$ , where  $r$  and  $R$  denote the radial coordinate and the radius of the cuvette, and the consecutive zeros of  $J_0(x)$  are given as  $x_0 \approx 2.4048$ ,  $x_1 \approx 5.5201$ ,  $x_2 \approx 8.6537$ ,  $x_3 \approx 11.7915$ ,  $x_4 \approx 14.9309$ , cf. Ref.<sup>34</sup>. We would like to point out here that mode  $i = 0$  shown in Fig. 10 will be excluded from further consideration of the surface oscillations in the cuvette, as volume conservation cannot be fulfilled in the case of a single node at the wall. In the following, we assume that the eigenmode  $F_i(r)$  of the cuvette is characterized by  $i$  nodes in  $0 < r < R$ .

When considering only the height variation in the center of the cell at  $r = 0$  mm, using  $F_i(0) = 1$ , Eq. (14) reduces to

$$\Delta h(0, t) = \Delta h_\infty(0) + \sum_{i=1}^{\infty} A_i \cos(2\pi f_i t + \delta_i) e^{-\gamma_i t}. \quad (15)$$

Initially, due to the approaching magnet, beside a static surface deformation, a set of different radial eigenmodes  $F_i(r)$  with frequencies  $f_i$  is excited. However, higher modes, characterized by a large number of nodes and a large oscillation frequency, can be expected to be damped by viscosity more strongly than those of a smaller index  $i$ . Thus, it appears likely that a mode with a single node at the surface is least damped and therefore visible at later points in time. Qualitatively, this mode is the same shape as mode 1 of the drum shown in Fig. 10. These arguments obtain further support from a more detailed observation of the surface deformation in the experiment in the outer part of the cuvette. As shown in Fig. 11, the temporal variation in the node position decays over time, and an asymptotic value of the node is established near  $r \approx 15$  mm. This result is in full agreement with the simulation result shown in Fig. 12 where the least damped mode is made visible at a late stage in the oscillations.

Next, we discuss the frequencies of the surface waves. All experiments show surface oscillations that are dominated by a single frequency which can be traced back to the  $i = 1$  mode. In this case, Eq. (15) can be used to fit the oscillatory behavior  $\Delta h(0, t)$  in both the experiments and the simulation, when the focus is restricted to the interval  $4 \text{ s} < t < 10 \text{ s}$  where the single mode behavior also dominates in the simulations. While  $A$  and  $\Delta h_\infty$  were

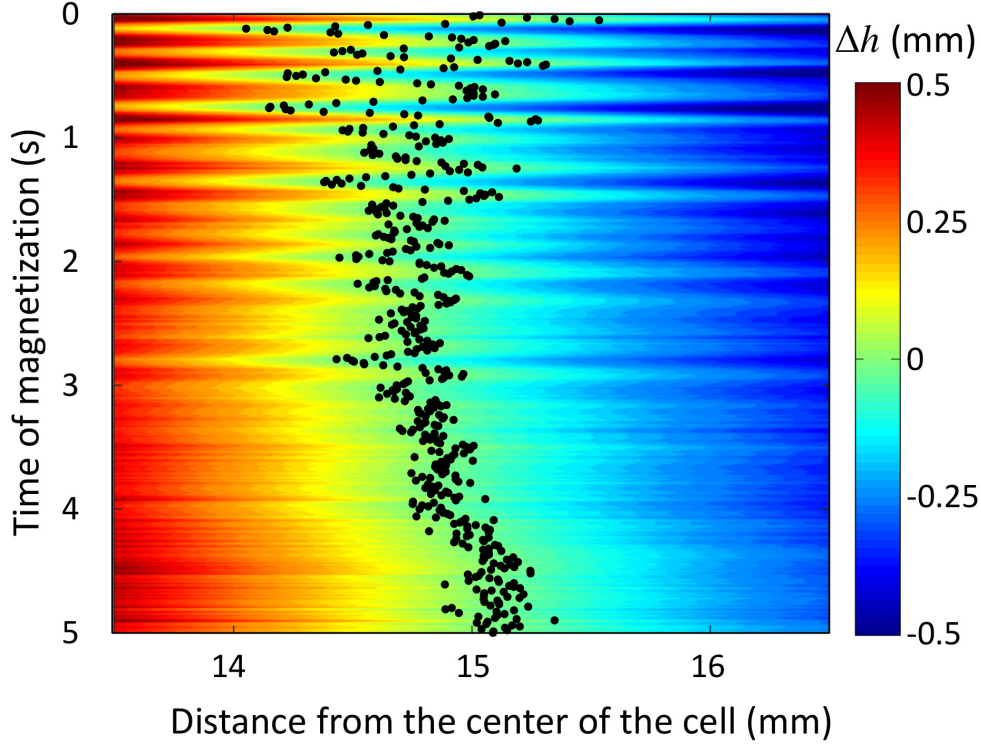


FIG. 11. Temporal behavior of the surface height  $\Delta h$  in experiment with a 0.75 M Dy(III) solution. An outer part of the cuvette ( $13.5 \text{ mm} < r < 16.5 \text{ mm}$ ) is shown, within which the surface wave has a node near  $r = 15 \text{ mm}$ . The black dots shown mark the temporal position of the node at which  $\Delta h - \Delta h_\infty = 0$  holds.

plotted in Fig. 5, the dominant frequencies are shown in Fig. 8. Here we note a decrease in the frequency from about  $f = 6 \text{ Hz}$  at  $c = 0$  to about  $f = 4 \text{ Hz}$  at  $c = 1 \text{ M}$  with an increasing  $\text{Dy}^{3+}$  concentration.

While only the  $i = 1$  mode has been identified in the experiments, higher harmonics which also possess higher frequencies than mode  $i = 1$  are visible in the simulations at the early stage. To understand why this behavior is not observed in the experiment, the frequency of the magnetic excitation is estimated. It roughly follows from the time it takes to approach the magnet, i.e.  $f_{\text{excitation}} \sim 1/\Delta t_{\text{approach}}$ . For the fast case,  $f_{\text{excitation}} \sim 1.3 \text{ Hz}$  is obtained, which is well below the observed oscillation frequency of mode  $i = 1$ . Consequently, the approaching speed of the magnet in the experiments is too slow to excite additional higher harmonics.

In the following, based on the oscillation frequencies  $f$  measured and the dispersion

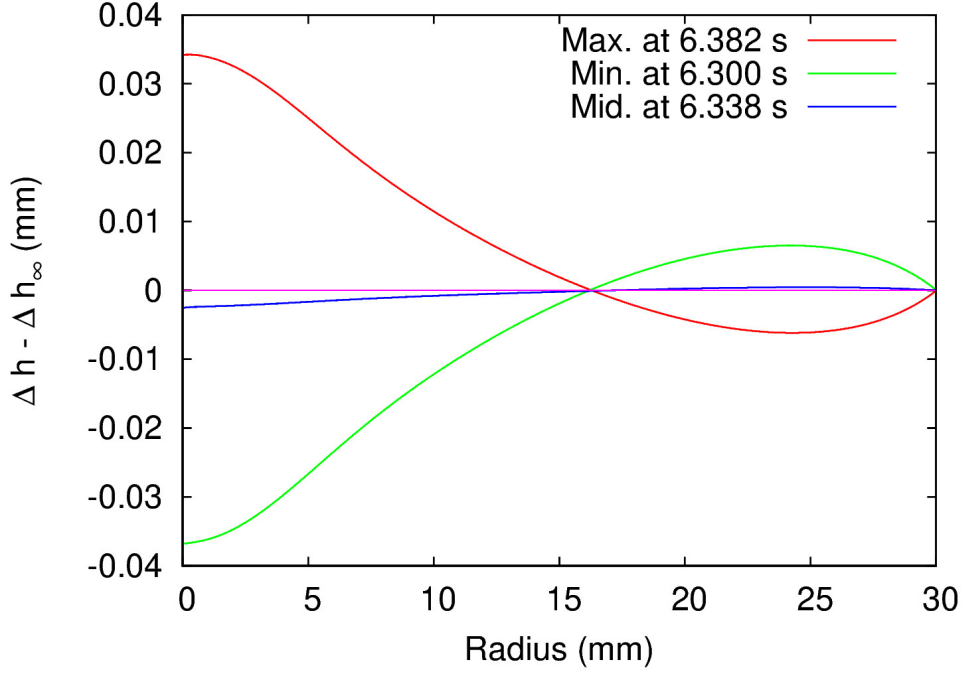


FIG. 12. Variation in the difference of surface deformation with respect to the static surface shape at later points in time near  $t = 6.3$  s where  $\Delta h(0)$  is minimum, maximum and approximately zero. Simulation result,  $c = 0.5$  M.

relations (10)-(11), we calculate the corresponding wave numbers  $k$  and wavelengths  $\lambda = 2\pi/k$  of the oscillations. We will further discuss the contributions of the different terms of the dispersion relations. The results are summarized in Table II. For the case of pure water, the measured oscillation frequency corresponds to a wavelength of  $\lambda = 53$  mm and, according to the dispersion relation (10), a wave number of  $k=118 \text{ m}^{-1}$ . As can be seen, the surface-tension-related term  $\sigma/\rho \cdot k^3$  is only of minor importance compared to the gravity-related term  $g \cdot k$ .

For the  $\text{DyCl}_3$  solutions studied, the dispersion relation (11) applies, where the gravitational acceleration is modified to its effective value  $g_{\text{eff}}$ . According to Equation (12), it holds that

$$g_{\text{eff}} = \frac{\chi_{\text{sol}}}{\rho\mu_0} B \frac{\partial B}{\partial z}, \quad (16)$$

where the values of the magnetic flux density and its gradient at the center axis  $r = 0$  are calculated at  $z = 0$ . Based on the numerical result shown in Fig. 1 b, the magnitude of the magnetic flux density is approximated as

$$B(z) = B_{\text{max}} e^{\alpha(z-z_0)}, \quad (17)$$



TABLE II. The oscillation frequencies  $f$  measured for the different solutions and related quantities derived from the dispersion relations (10) or (11). For the  $\text{DyCl}_3$  solutions,  $g$  is replaced by the value  $g_{\text{eff}}$  resulting from Eq. (16). Additionally, for three preset wave numbers, the quantities resulting from Eq. (10) are calculated inversely. The material parameters used in the calculations are given in Section IV.

Case	$f$ [ $\text{s}^{-1}$ ]	$\lambda$ [m]	$k$ [ $\text{m}^{-1}$ ]	$g$ [ $\text{ms}^{-2}$ ]	$g \cdot k$ [ $\text{s}^{-2}$ ]	$\frac{\sigma}{\rho} \cdot k^3$ [ $\text{s}^{-2}$ ]	$\frac{\chi_{\text{sol}}^2}{4\rho} \frac{B_0^2}{\mu_0} k^2$ [ $\text{s}^{-2}$ ]
$\lambda = D/2$	8.28	0.030	209	9.81	2054	651	\
$\lambda = 2D/3$	6.78	0.040	157	9.81	1540	275	\
$\lambda = D$	5.30	0.060	105	9.81	1027	81	\
$\text{H}_2\text{O}$	5.70	0.053	118	9.81	1162	120	\
$c_{\text{Dy(III)}} = 0.25$ M	5.41	0.050	126	8.06	1018	137	0.028
$c_{\text{Dy(III)}} = 0.5$ M	5.29	0.044	142	6.35	899	206	0.145
$c_{\text{Dy(III)}} = 0.75$ M	4.79	0.043	147	4.85	712	192	0.337
$c_{\text{Dy(III)}} = 1$ M	4.08	0.044	141	3.48	492	164	0.537

where  $B_{\text{max}} = 0.7558$  T and  $\alpha = 220$   $\text{m}^{-1}$  denote the flux density at the magnet surface and the vertical downward decay rate of the field. The values of  $g_{\text{eff}}$  obtained are listed in Table II. Despite the continuous decrease in  $g_{\text{eff}}$  with increasing concentration, the gravity term in the dispersion relation still dominates the surface tension even at the largest concentration investigated. Finally, the last term of the dispersion relation (11), which describes a magnetic correction, is negligible at all concentrations investigated when compared to the aforementioned terms of gravity and surface tension.

Table II further shows that as the salt concentration increases, the decrease in the oscillation frequencies measured is accompanied by a moderate decrease in the wavelength. At  $c = 0.5$  M, based on the dispersion relation (11), a wavelength of 44 mm is found. This value is in very good agreement with the simulation result of the least damped oscillation mode shown in Fig. 12. Here, a wavelength of about 45 mm can be extracted, which is measured as twice the distance between  $r = 0$  and the position of the extremum of the amplitude.

In order to study the sensitivity of the oscillation frequency with respect to the wave number, the upper three lines in Table II show cases where wave number values are preset, and the inversely resulting terms of Eq. (10) and the oscillation frequencies are calculated.

As expected, the frequency and wave number in the case of pure water lie between the values obtained for  $\lambda = 2D/3$  and  $\lambda = D$ . Moreover, as already seen above, the magnetic term in the dispersion relation (11) is negligible. Therefore, in Fig. 8, for the three cases of preset wave numbers the frequencies resulting from Eq. (11) are plotted, neglecting the magnetic term. It can be seen that in the range of salt concentrations investigated here the oscillation frequencies obtained for the two cases of  $\lambda = 2D/3$  and  $\lambda = D$  act as upper and lower boundaries for the oscillation frequencies measured and obtained by numerical simulations. As the salt concentration increases, the reduction in the oscillation frequency is accompanied by a moderate decrease in the wave number, as also listed in Table II.

The dispersion relations (10) and (11), as mentioned before, are valid under the side condition  $kH > 1$ , where  $H$  denotes the height of the filled vessel. As can be seen, this condition is clearly fulfilled in all cases. The dispersion relations (10) and (11) furthermore exclude any viscous effects which might also influence the oscillation frequency, beside the temporal damping of the oscillation amplitude. However, the frequency correction factor derived in<sup>35</sup> results in a nearly unchanged oscillation frequency in our case, as  $\sqrt{1 - (2\eta k^2/(\rho\omega))^2} \approx 1$ . This is also confirmed in surface-wave damping experiments performed in a vessel of a similar size to that used here, where the frequency of the least damped mode was reported to be nearly unchanged<sup>32</sup>.

Analogously to the normal field instability of ferrofluids, the surface elevation can be explained by minimizing the total energy of the system. The magnet elevates the paramagnetic liquid, causing the magnetic energy to be lowered, since the fluid can be magnetized more easily than air. On the other hand, it requires energy to lift the fluid and to form a new interfacial area. The formation of the solitary wave of paramagnetic liquid causes a reduction in the magnetic energy, but the surface energy and the potential energy of the liquid are increased. The undulation in our system is determined by a gravity-driven standing wave, associated with the effective gravitational acceleration due to the magnetic field gradient force. The deformation is time-dependent and exhibits an oscillatory behavior, with the  $i = 1$  mode proving to be the dominant and least damped mode.

## VII. PARAMAGNETIC LIQUID AS A SWITCH

The surface deformation of ferrofluids finds numerous practical application in magnetic seals and bearings. In contrast, for paramagnetic liquids, the effect has not yet been utilized to any great extent. This section describes a possible application of this research, consisting in using the paramagnetic liquid as a thermal or electrical switch. The principle is to use the ionic solution as an electrical or thermal conductor, and silicon oil as electrical or thermal insulator. The principle of a thermal or electrical switch was visually tested. For this purpose, the cell with a square cross-section of  $10\text{ mm} \times 10\text{ mm}$  and a height of  $45\text{ mm}$  was filled with 2 different liquids:  $1\text{ M DyCl}_3$  solution at the bottom and paraffin oil (Fluka Analytical, CAS No. 8012-85-1) on top of it. The volume of oil was  $0.25\text{ mL}$ ; the rest was filled with paramagnetic ionic solution. To keep the meniscus between the two liquids as small as possible, a hydrophobic acrylic glass cell was chosen and the interface was adjusted by adding the two liquids alternately. The cell was covered with a  $0.13\text{ mm}$  thick coverslip. The same magnet configuration was used as in experiments involving the observation of free surface. Vertically symmetrical planes of the magnet and cell were aligned and the magnet moved in the vertical direction. The magnet rests  $35\text{ mm}$  from the coverslip in the demagnetization phase and  $0.1\text{ mm}$  away in the magnetization phase.

Representative pictures of the concept are collected in Fig. 13. Only the middle part of the cell is shown. Fig. 13-a presents the state with no thermal/electrical contact, since the paraffin oil rests on the  $\text{Dy(III)}$  solution without interruption. Neither liquid is influenced by a magnetic field; the bottom of the magnet is  $35\text{ mm}$  above the cover slip. When the magnet is near enough, the paramagnetic ionic solution is attracted (Fig. 13-b) and the level of paramagnetic solution approaches the cover slip in the central part of the cross section. Hence, the paraffin oil is pushed to the walls of the cell. When the paramagnetic solution comes into contact with the cover glass (Fig. 13-c) the thermal/electrical contact is possible if the cover glass is replaced by an electrode. When the magnet is removed, the liquids separate according to their densities and there is no contact between the  $\text{DyCl}_3$  solution and the cover slip; hence, the switch is turned off. Fig. 13-d shows the distribution of liquids shortly before the contact is cut off. The design and geometries of the switch can be adjusted according to the desired requirements. This offers the possibility of a wide range of applications, from the size of a microchip to macro dimensions.

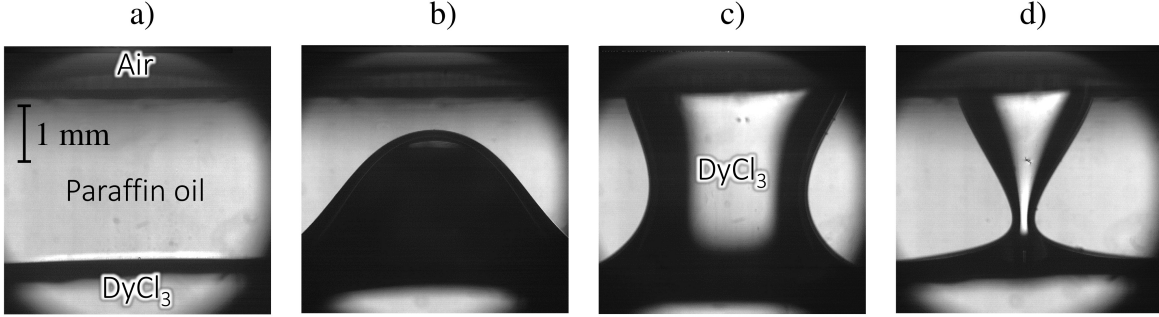


FIG. 13. Principle of an electrical/thermal switch with paraffin oil and paramagnetic liquid: a) no magnet is applied, b) the magnet is approaching, c) the magnet is at its end position and the Dy(III) solution is in contact with the cover slip, d) demagnetization phase.

## VIII. CONCLUSION

This work investigated the response of the free surface of a paramagnetic liquid subjected to an inhomogeneous magnetic field which changes over time. The magnetic actuation results in deformations of the interface. The free surface was found to oscillate with a specific frequency, which is defined by the concentration of the paramagnetic ions, and which is independent of the velocity of the permanent magnet. The frequencies measured in experiments are slightly lower than the data from the numerical simulation. However, the surface elevation in the center and the morphology of the surface in the simulation and experiment agree well. Hence, the theoretical model provides a good description of the reaction of the paramagnetic liquid's free surface evoked by a moderate magnetic field gradient. It was further shown that the amplitude of the surface oscillations caused by a magnetic field, in contrast to the frequency, depends on both the concentration and the magnet velocity. The temporal dynamics of the height difference beneath the center of the magnet can be mathematically described by an exponentially decaying cosine wave after higher modes are damped out. Finally, as a potential application, an electronic switch was demonstrated which utilizes the interfacial instability between a paramagnetic liquid and a paraffin oil.

## ACKNOWLEDGMENTS

We are grateful to Xinghao Yang for contributions to the simulations and to Gerrit Maik Horstmann for fruitful discussions. This work is supported by the German Aerospace Center (DLR) with funds provided by The Federal Ministry for Economic Affairs and Energy (BMWi) due to an enactment of the German Bundestag under Grant No. 50WM1741 (project SESIMAG II).

## REFERENCES

- <sup>1</sup>J. Coey, F. Rhen, P. Dunne, and S. McMurry, *J Solid State Electrochem* (2006), DOI 10.1007/s10008-006-0254-4.
- <sup>2</sup>G. Mutschke, K. Tschulik, T. Weier, M. Uhlemann, A. Bund, and J. Fröhlich, *Electrochimica Acta* **55**, 9060 (2010).
- <sup>3</sup>M. Fujiwara, D. Kodoi, W. Duan, and Y. Tanimoto, *The Journal of Physical Chemistry B* **105**, 3343 (2001).
- <sup>4</sup>X. Yang, K. Tschulik, M. Uhlemann, S. Odenbach, and K. Eckert, *The Journal of Physical Chemistry Letters* **3**, 3559 (2012).
- <sup>5</sup>O. Y. Gorobets, Y. I. Gorobets, I. Bondar, and Y. A. Legenkiy, *Journal of Magnetism and Magnetic Materials* **330**, 76 (2013).
- <sup>6</sup>B. Pulko, X. Yang, Z. Lei, S. Odenbach, and K. Eckert, *Applied Physics Letters* **105**, 232407 (2014).
- <sup>7</sup>A. Franczak, K. Binnemans, and J. Fransaer, *Physical Chemistry Chemical Physics* **18**, 27342 (2016).
- <sup>8</sup>K. Koleczyk, D. Kutyla, M. Wojnicki, A. Cristofolini, R. Kowalik, and P. Zabinski, *Magnetohydrodynamics* **52**, 541 (2016).
- <sup>9</sup>Z. Lei, B. Fritzsche, and K. Eckert, *The Journal of Physical Chemistry C* **121**, 24576 (2017).
- <sup>10</sup>I. R. Rodrigues, L. Lukina, S. Dehaeck, P. Colinet, K. Binnemans, and J. Fransaer, *The Journal of Physical Chemistry Letters* **8**, 5301 (2017).
- <sup>11</sup>Z. Lei, B. Fritzsche, and K. Eckert, *Physical Review E* **101**, 013109 (2020).

- <sup>12</sup>K. Chie, M. Fujiwara, Y. Fujiwara, and Y. Tanimoto, The Journal of Physical Chemistry B **107**, 14374 (2003).
- <sup>13</sup>M. Fujiwara, K. Chie, J. Sawai, D. Shimizu, and Y. Tanimoto, The Journal of Physical Chemistry B **108**, 3531 (2004).
- <sup>14</sup>M. Fujiwara, K. Mitsuda, and Y. Tanimoto, The Journal of Physical Chemistry B **110**, 13965 (2006).
- <sup>15</sup>M. López-López, P. Kuzhir, S. Lacis, G. Bossis, F. González-Caballero, and J. D. Durán, Journal of Physics: Condensed Matter **18**, S2803 (2006).
- <sup>16</sup>M. D. Cowley and R. E. Rosensweig, Journal of Fluid Mechanics **30**, 671 (1967).
- <sup>17</sup>A. Engel, A. Lange, H. Langer, T. Mahr, and M. Chetverikov, Journal of Magnetism and Magnetic Materials **201**, 310 (1999).
- <sup>18</sup>A. Lange, H. Langer, and A. Engel, Physica D: Nonlinear Phenomena **140**, 294 (2000).
- <sup>19</sup>S. Odenbach, Journal of Magnetism and Magnetic Materials **170**, 309 (1997).
- <sup>20</sup>T. Vieu and C. Walter, Journal of Fluid Mechanics **840**, 455 (2018).
- <sup>21</sup>N. Hirota, T. Homma, H. Sugawara, K. Kitazawa, M. Iwasaka, S. Ueno, H. Yokoi, Y. Kaku-date, S. Fujiwara, and M. Kawamura, Japanese journal of applied physics **34**, L991 (1995).
- <sup>22</sup>A. Catherall, K. A. Benedict, P. King, and L. Eaves, Physical Review E **68**, 037302 (2003).
- <sup>23</sup>J. M. D. Coey, R. Aogaki, F. Byrne, and P. Stamenov, Proceedings of the National Academy of Sciences **106**, 8811 (2009).
- <sup>24</sup>R. Rosensweig, *Ferrohydrodynamics*, Dover Books on Physics (Dover Publications, 1997).
- <sup>25</sup>B. Berkovskii and L. Orlov, Magn. Gidrodin (1973).
- <sup>26</sup>S. H. Lamb, *Hydrodynamics*, 6th ed. (Cambridge University Press, 1993).
- <sup>27</sup>R. Zelazo and J. Melcher, Journal of Fluid Mechanics **39**, 1 (1969).
- <sup>28</sup>A. Habenschuss and F. H. Spedding, The Journal of Chemical Physics **70**, 2797 (1979).
- <sup>29</sup>C. W. Hirt, A. A. Amsden, and J. Cook, Journal of computational physics **14**, 227 (1974).
- <sup>30</sup>J. Donea, J.-P. Ponthot, and A. Rodriguez Ferran, “Encyclopedia of computational mechanics,” (2004).
- <sup>31</sup>T. Meinel, *Experimentelle und numerische Untersuchungen der Deformation freier Oberflaechen paramagnetischer Salzloesungen unter dem Einfluss von Magnetfeldern*, Student Report (TU Dresden, Fac. Mech. Eng., 2017).
- <sup>32</sup>D. M. Henderson and J. Miles, Journal of Fluid Mechanics **275**, 285 (1994).
- <sup>33</sup>R. Kidambi, Journal of Fluid Mechanics **627**, 323 (2009).

<sup>34</sup>C. Jenkins and U. Korde, Journal of Sound and Vibration **295**, 602 (2006).

<sup>35</sup>F. Denner, Physical Review E **94**, 023110 (2016).